Journal of Geophysical Research: Atmospheres

RESEARCH ARTICLE
10.1029/2017JD027508

# Cloud-Scale Droplet Number Sensitivity to Liquid Water Path in Marine Stratocumulus

**Simon P. de Szoeke**[1], **Kathryn L. Verlinden**[1], **and David Covert**[2]

[1]College of Earth, Ocean, and Atmospheric Sciences, Oregon State University, Corvallis, OR, USA, [2]Department of Atmospheric Sciences, University of Washington, Seattle, WA, USA

**Key Points:**
- Stratocumulus clouds show lower liquid water path for greater cloud droplet number concentration, contrary to the cloud lifetime effect
- Cloud variance factors into two orthogonal modes: 68% macrophysical and 28% microphysical
- Dynamic and thermodynamic forcings drive macrophysical variability that controls droplet number

**Correspondence to:**
S. P. de Szoeke,
sdeszoek@coas.oregonstate.edu

**Citation:**
de Szoeke, S. P., Verlinden, K. L., & Covert, D. (2018). Cloud-scale droplet number sensitivity to liquid water path in marine stratocumulus. *Journal of Geophysical Research: Atmospheres, 123*, 5320–5334. https://doi.org/10.1029/2017JD027508

Received 25 JUL 2017
Accepted 17 APR 2018
Accepted article online 26 APR 2018
Corrected 01 JUN 2018
Published online 17 MAY 2018

This article was corrected on 11 JUN 2018. See the end of the full text for details.



**Abstract** Cloud droplet number concentration ($N_c$) is retrieved from remotely observed marine stratocumulus cloud liquid water path (LWP), cloud optical depth ($\tau_c$), and cloud thickness, using an optical model that assumes liquid water content (LWC) increases linearly from cloud base. Assuming that LWC is vertically uniform would underestimate $\tau_c$ by 5% and $N_c$ by 14%. Individual retrievals of $N_c$ from 10-min averages vary by orders of magnitude from long-term averages. Surface cloud condensation nuclei (CCN) number concentration $N_{CCN}$ is weakly but significantly correlated with $N_c$ ($R = 0.3$) for the day leading and 6 hr following $N_c$. Consistent with coalescence and drizzle scavenging cloud droplets, lag correlations show that $N_c$ decreases for 1 hr after the peak area-average rain rate. Greater observed LWP for lower $N_c$ [d(log $N_c$)/d(log LWP) = −2.3] is consistent with enhanced entrainment drying of clouds with greater $N_c$ and consistent with removal of $N_c$ by thicker clouds with more coalescence and drizzle. Stronger precipitation in clouds with greater $N_c$ is the opposite sensitivity as expected were LWP to be controlled by the "cloud lifetime" indirect aerosol effect. The strong sensitivity of $N_c$ to LWP suggests that cloud dynamic and thermodynamic forcings drive macrophysical variability that controls $N_c$ in southeastern tropical Pacific stratocumulus clouds. Regressions are relatively insensitive to assumptions about the covariance of errors among the sensors.

## 1. Introduction

The fate of brightly reflective yet relatively warm low clouds strongly affects the response of climate to greenhouse gases, so low clouds are a leading source of uncertainty for climate projections. The optical properties, lifetime, and extent of low clouds depend on interactions between the macrophysical amount of condensate, and the microphysical number of droplets $N_c$ over which that liquid water is distributed. Higher droplet number concentration $N_c$ implies greater cloud droplet cross-sectional area, more scattering, and greater cloud albedo (Twomey, 1974).

All else being equal, it has been hypothesized that fewer cloud droplets in competition for the same total volume of liquid water ought to grow larger, coalesce, and precipitate more effectively (Albrecht, 1989). More aerosols and higher $N_c$ increase liquid water path (LWP) by delaying drizzle. This is known as the *cloud lifetime* effect. The suppression of drizzle has been observed in marine stratus and shallow cumulus clouds (Ferek et al., 2000; Hudson et al., 2009; Hudson & Yum, 2001). If instead precipitation is governed by LWP, then coalescence and rainout at greater LWP will reduce $N_c$ (Hudson et al., 2015; Wood et al., 2012). Large eddy simulations (LES) of stratocumulus clouds demonstrate a third process: Increased $N_c$ reduces droplet size, thus enhancing evaporation, turbulence, and entrainment at cloud top. In these simulations entrainment drying dominates the (Albrecht, 1989) cloud lifetime effect when the air above the inversion is sufficiently dry (Jiang et al., 2002). This entrainment drying reduces precipitation, which in turn reduces subcloud turbulence, thus reducing the resupply of moisture to the cloud from the surface layer. This mechanism of enhanced entrainment drying of clouds with higher $N_c$ is illustrated schematically in Figure 1. On the other hand, sedimentation of cloud droplets at cloud top reduces droplet evaporation and entrainment drying near the inversion (Ackerman et al., 2004; Bretherton et al., 2007). Wood (2006) examined the opposing sensitivity of entrainment and precipitation drying to $N_c$ in a mixed layer model, finding that the effect of entrainment dominates and cloud albedo decreases with higher $N_c$, for clouds with bases below 400 m. Consistent with either LWP controlling $N_c$ or with $N_c$-enhanced entrainment drying, LWP was found to be anticorrelated with $N_c$ in the southeastern tropical Pacific (Painemal & Zuidema, 2010; Wood et al., 2012) and in northeastern subtropical Pacific marine stratocumulus clouds offshore of California (Twohy et al., 2005).

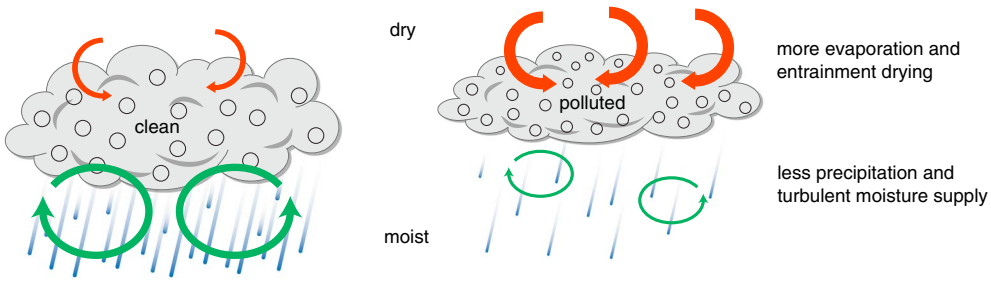


**Figure 1.** Schematic illustrating how "polluted" clouds with more aerosols dry more by entrainment than clean clouds dry by precipitation (Ackerman et al., 2004; Jiang et al., 2002). Entrainment of dry air is enhanced by more evaporation of smaller droplets, and less precipitation stirs up less subcloud moisture from the surface boundary layer for the polluted cloud.

Climate models need to adequately represent the effect of microphysical-macrophysical interactions, yet the interactions among cloud amount, LWP, aerosols, and $N_c$, use uncertain and unconstrained parameterizations. Intentional seeding of marine stratocumulus clouds with cloud condensation nuclei (CCN) in order to increase their albedo, extent, and/or lifetime to mitigate climate change has been tested in climate models (Jones et al., 2009; Rasch et al., 2009). Preindustrial to industrial climate simulations are tuned to match Earth's historically observed temperature and implied heat balance, yet there is considerable variety in the direct and cloud indirect aerosol radiative effects among models. Aerosol-radiative effects and aerosol-cloud indirect effects are the leading uncertainty in climate models because the preindustrial aerosol burden is unknown, and interactions among clouds and aerosols are not well constrained (Carslaw et al., 2013; Ghan et al., 2016; Seinfeld et al., 2016).

The range of scales for climate-cloud-aerosol interactions spans 14 orders of magnitude from the scale of microphysics ($10^{-8}$ m) to the scale of regional climate ($10^{6}$ m). Aerosols, especially CCN, affect clouds on the scales of molecular dissipation of their turbulent motion. Interactions on the mesoscale and smaller include the cloud scale, turbulence, and microphysics. These must be parameterized in climate models that project global and regional scale responses of climate and clouds to emissions. The microphysical-macrophysical cloud interactions are notoriously difficult to deconvolve (Gryspeerdt et al., 2016; Stevens & Feingold, 2009). Cloud behavior resulting from regime-specific interactions in the present climate provide opportunities to reduce uncertainty and constrain cloud-aerosol interactions.

This paper is concerned with measuring the cloud-scale (order 1 km) properties of marine boundary layer clouds. The retrievals, averaged over 10 min, represent roughly 4 km of stratocumulus clouds transiting directly overhead. On this scale, we investigate the $N_c$ behavior in relation to integrated LWP, cloud thickness $\Delta z$, and cloud optical depth $\tau_c$. In section 2 we introduce measured quantities representative of southeast Pacific marine stratocumulus clouds during VAMOS Ocean Cloud Atmosphere Land Study (VOCALS; Allen et al., 2011; Wood et al., 2011). In section 3 we describe the retrieval of $N_c$ from these measured quantities. Different respective averaging kernels for remotely sensed cloud transmission ratio, $\Delta z$, and LWP lead to discrepancies in the remote sensing retrievals. We estimate the empirical covariance structure of the true and error quantities in section 4. In section 5 we estimate the sensitivity of $N_c$ to LWP, based on the observed relationships among $\tau_c$, $\Delta z$, and LWP. Section 6 summarizes the conclusions.

## 2. Measurements

Observations of southeastern Pacific stratocumulus clouds were made along 20°S, 75°–85°W from a ship, the research vessel *Ronald H. Brown*, during 19 October to 1 December 2008 (de Szoeke et al., 2010, 2012). We use LWP from a microwave radiometer (Zuidema et al., 2005, 2012), surface solar radiation from a pyranometer, cloud top from the National Oceanic and Atmospheric Administration (NOAA) W-band cloud radar (3.4-mm wavelength; Moran et al., 2012), and cloud base from a Vaisala (lidar) ceilometer. These measurements, as well as those of surface meteorology and fluxes, were carried out by the NOAA Earth System Research Laboratory Physical Sciences Division (PSD). The PSD ship data for research cruises to the Woods Hole Ocean Reference Station buoy at 20°S, 85°W are averaged over 10-min windows as described in de Szoeke

et al. (2010, 2012). Cloud thickness $\Delta z$ is the difference between the radar cloud top and the lidar cloud base. There are 1,289 contemporaneous 10-min average realizations of daylight LWP, $\tau_c$, and cloud thickness that permit retrieval of $N_c$. LWP is dominated by cloud liquid water. The total drizzle water volume is $<30$ g/m$^2$, even for an exaggerated drizzle scenario (Zuidema et al., 2005). The effect on the LWP due to Mie scattering by larger drizzle drops is less than the instrumental uncertainty.

The number-size spectra of aerosol particles at 18 m above the ocean surface was measured at 60% relative humidity aboard the ship every 10 min in 17 equal log-spaced diameter bins between 20 and 800 nm with two differential mobility particle sizers operating in parallel. Cloud activation of aerosols depends on their diameter, hygroscopicity, and the environmental supersaturation, which in turn depends on updraft speed. Particles with diameter above 80 nm were measured with an aerosol mass spectrometer and were highly soluble (i.e., of hygroscopic composition; Hawkins et al., 2010). As an approximation for the number concentration of CCN $N_{CCN}$ below cloud base, we use the integral of particle number concentration greater than the critical diameter for droplet nucleation at 0.6% supersaturation derived from aerosol size spectra. Area-averaged rain rate is estimated from a C-band weather radar (Burleyson et al., 2013).

## 3. Retrievals

When the solar elevation angle is greater than 6° (cosine of zenith angle $\mu_0 > 0.1$), $N_c$ and effective radius $r_e$ of the clouds are retrieved from the LWP, $\Delta z$, and transmission ratio of downwelling solar radiation by clouds, compared to clear sky (de Szoeke et al., 2012). The downwelling solar radiation $S$ at the surface is an average of the clear-sky solar radiation $S_0$ and overcast solar radiation $S_1$, weighted by the cloud fraction $f$ from the ceilometer,

$$S = (1–f)S_0 + fS_1. \tag{1}$$

Thus, the overcast solar transmission ratio $\gamma \equiv S_1/S_0$ is estimated for the ensemble of scenes for which cloud is present, by scaling the observed transmission ratio $S/S_0$ by the cloud fraction $f$,

$$\gamma \equiv S_1/S_0 = 1–(1–S/S_0)/f.$$

We note that the ceilometer has a narrow field of view directly overhead, while the observed solar radiation $S$ is a hemispheric average. The ceilometer cloud fraction and solar radiation are averaged for 10 min, but in cases when the cloud fraction is low, the difference in the fields of view of the instruments introduces significant random errors.

### 3.1. Estimating Optical Depth From the Transmission Ratio

To relate the optical depth of the cloud $\tau_c$ to the overcast solar total transmission ratio of direct plus diffuse radiation, $\gamma = \gamma_{dir} + \gamma_{diff}$, we add the direct solar transmission to the diffuse solar transmission ratio $\gamma_{diff}$ of Barnard and Long (2004; BL04). The formulations of the direct and diffuse radiation are based on the δ-Eddington approximation (Joseph et al., 1976). The direct transmission ratio is

$$\gamma_{dir} = \exp\left(-\tau_c\left(1 - g^2\right)/\mu_0\right), \tag{2}$$

with cloud optical depth $\tau_c$ transformed by the factor $(1 - g^2)$, where $g = 0.85$ is the asymmetry parameter, or ratio of forward to backward scattering for the droplets.

BL04 relates $\tau_c$ to diffuse transmission ratio $\gamma_{diff}$ for $\tau_c$ greater than about 10,

$$\tau_c = \exp\left[2.15 + A + 1.91\ \operatorname{arctanh}\left(1–1.74\gamma_{diff}\mu_0^{-0.25}\right)\right], \tag{3}$$

where $A = 0.05$ is the ocean surface albedo. This expression fits broadband discrete ordinate calculations optimally. To get diffuse transmission ratios appropriate for smaller $\tau_c$, we multiply $\gamma_{diff}$ in 3 by the factor $1 - \phi\gamma_{dir}$. BL04 equation 3 gives the factor $\phi = 1 + 3(A - 1)(1 - g)/(2 + 3\,\mu_0)$. The second term of this factor is of order 0.1. Neglecting this second term, $\phi = 1$. Then replacing $\gamma_{diff}$ in (3) by $\gamma_{diff}(1 - \gamma_{dir})$ gives

$$\tau_c = \exp\left[2.15 + A + 1.91\ \operatorname{arctanh}\left(1–1.74\gamma_{diff}(1 - \gamma_{dir})\mu_0^{-0.25}\right)\right]. \tag{4}$$

In this case, the transmission $\gamma$ is unity for $\tau_c = 0$.

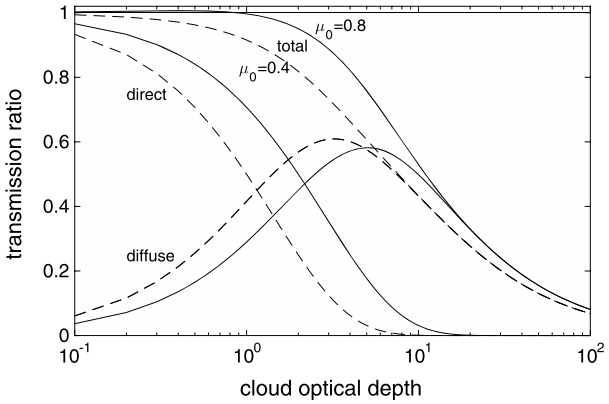


**Figure 2.** Total, direct, and diffuse cloud transmission ratio as a function of cloud optical depth $\tau_c$ for cosine of zenith angle $\mu_0$ = 0.4 (dashed) and 0.8 (solid).

The optical depth $\tau_c$ given by (4) is a smooth but transcendental function of $\gamma$. For $\tau_c > 0.9$, $\gamma$ decreases monotonically with $\tau_c$. We find $\tau_c$ numerically from $\gamma$ by interpolating with a lookup table. Figure 2 shows the total, direct, and diffuse transmission ratios as a function of optical depth for $\mu_0$ = 0.4 and 0.8.

Our method of calculating $\tau_c$ from total transmission $\gamma$, adapted from the optical model of BL04, preserves the independence of LWP for inferring microphysical-macrophysical interactions. The statistical results from the microphysical retrieval in this paper are not sensitive to the optical depth calculation. Substituting the total (diffuse plus direct) downwelling solar transmission for the diffuse transmission ratio in (3) does not strongly affect the inferred empirical sensitivities for the optically thick clouds in this study.

### 3.2. LWP and Cloud Thickness

Since LWP and $\Delta z$ are independently retrieved, their relationship can be assessed. LWP would depend on the square of $\Delta z$ if liquid water content (LWC) increased linearly (moist adiabatically from 0 at cloud base, for example) at a constant rate $\Gamma$ for all clouds. Regression of the logarithms of LWP and $\Delta z$ (Figure 3) yield a slightly weaker power, LWP $\propto (\Delta z)^{1.8}$, however. Since LWP is the vertical integral of LWC, this implies that LWC increases slightly less steeply than linearly—as height to the 0.8 power on average, or that clouds have a linear LWC gradient that depends weakly negatively on the thickness as $(\Delta z)^{-0.2}$.

The slightly less than quadratic dependence of LWP on cloud thickness could be because deeper clouds entrain more dry air, which warms them and dilutes their total water content. This is consistent with conceptual models of decoupled cloud-topped boundary layers (Wyant et al., 1997), where dry entrainment drives evaporation and separation of the radiatively driven cloud layer from the lifted condensation level of moist surface air. Decoupling leads to cumulus under stratocumulus, also known as scud clouds. Since these cumulus clouds need not reach all the way to the stratocumulus, LWP may be considerably less than expected assuming a saturated adiabatic cloud layer from the decoupled cumulus cloud base to the stratocumulus capping inversion. To avoid sampling the cloud base of cumulus under stratocumulus, we take the 85th percentile cloud base from the ceilometer. This procedure might undercount the contribution of intermittent cumulus clouds to the LWP. Cloud optical depth depends on both LWP and $\Delta z$, so we retain independent measurements of each despite their correlation ($R$ = 0.57; Figure 3). The 0.8-power dependence of LWC on thickness is approximated as a linear dependence in the optical calculations that follow. We also consider the effect of assuming a vertically uniform (0-power) LWC.

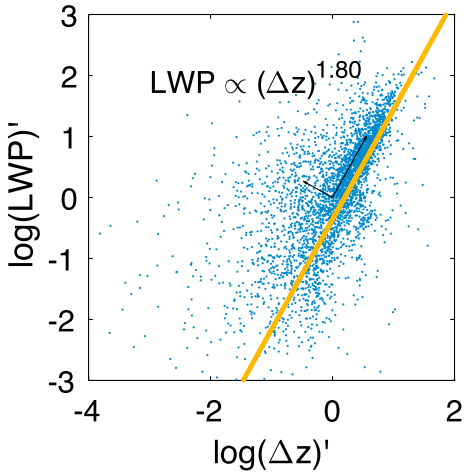


**Figure 3.** (a) Logarithm of LWP versus logarithm of cloud thickness $\Delta z$. Black vectors show eigenvectors of the covariance scaled by amplitude. The yellow line shows the regression describing LWP$\propto(\Delta z)^{1.8}$. LWP = liquid water path.

### 3.3. Microphysical Retrieval

The optical depth for a uniform cloud of thickness $\Delta z$ with lognormal droplet size distribution is (Dong et al., 1997)

$$\tau_c = Q_e\, \pi\, r_m^2\, \exp(2\sigma^2) N_c\, \Delta z,$$

where $Q_e$ = 2 is the extinction efficiency, $r_m = r_e \exp(-5\sigma^2/2)$ is the modal radius ($r_e$ is effective radius), and $\sigma$ = 0.35 is the lognormal width. Similarly integrating the extinction cross section for a cloud whose LWC increases linearly from LWC = 0 at cloud base, through the depth of the cloud, and integrates to the observed LWP gives

$$\tau_c = Q_e\, \pi^{1/3}\, \rho_w^{-2/3}\, \exp(-\sigma^2)\, (3/2)^{2/3}\, (3/5)\, N_c^{1/3}\, (\Delta z)^{1/3}\, (\mathrm{LWP})^{2/3}. \quad (5)$$

We assume a single vertically uniform droplet number concentration $N_c$ within the cloud. Effective radius $r_e$ increases with height, along with

LWC. Because proportionally more of the LWC is distributed to larger droplets at the top of the cloud, $\tau_c$ for linearly increasing LWC is $3 \times 2^{2/3}/5 = 0.95$ times that of the uniform-LWC cloud (cf. (5) with Dong et al., 1998 equation 7). Assuming uniform LWC would result in a 14% underestimate of $N_c$, relative to a cloud with linearly increasing LWC. This systematic underestimate is small compared to random errors.

Rearranging (5),

$$N_c = (\tau_c/\beta k)^3 (\mathrm{LWP})^{-2} (\Delta z)^{-1} \tag{6}$$

is found from 10-min averages of $\tau_c$, LWP, and $\Delta z$ with $\beta^3 = {Q_e}^3\, \pi\, {\rho_w}^{-2} \exp(-3\sigma^2)$, and $k^3 = (3/2)^2\,(3/5)^3$ for linearly increasing LWC. The effective radius $r_e$ is solved at each height from the uniform $N_c$ and linear assumed LWC profile.

We calculate the retrieval only for representative averages of solar transmission through cloud, requiring both high enough solar elevation (zenith angle $\theta < 84°$) and sufficient cloud fraction ($f > 0.2$). The total cloud transmission ratio $\gamma$ can only be found from $\tau_c$ by inverting equation (3) for diffuse transmission ratio over the range $0 < \gamma_{\mathrm{diff}} < (1.74)^{-1} \approx 0.57$. We assume that the lower bound is satisfied if $S_0 > 50$ W/m$^2$, that is, sufficiently greater than the error of the solar radiometer (5 W/m$^2$). The upper bound limits the retrieval to clouds that transmit no more than 0.57 of the diffuse radiation. The retrieval is not performed for $\gamma \geq 0.57$. The cloud microphysical retrieval is also only performed if the solar transmission $S/S_0 < 0.975$. Optical depths from our variant of the BL04 retrieval exceed those implied by the ground-based microphysical retrieval for marine stratocumulus of Dong et al. (1998, D98) by 0.4 in the mean and are correlated with D98 optical depths at $R = 0.96$. Further comparison with the D98 retrieval is presented in Appendix A.

### 3.4. Surface CCN $N_{CCN}$ and Cloud Droplet Number $N_c$

The distribution of the optically retrieved $N_c$ is compared with that of the number concentration of CCN ($N_{CCN}$) at 0.6% supersaturation, modeled from shipboard observations of the in situ aerosol size distribution and chemistry. Contemporaneous measurements of $\log(N_{CCN})$ are correlated with optically retrieved $\log(N_c)$ at $R = 0.34$, which, with 203 degrees of freedom, far exceeds the statistical significance criterion for a correlation distinct from 0. This estimate of degrees of freedom has been appropriately diminished by the one-lag autocorrelations of $\log(N_{CCN})$ and $\log(N_c)$ by the method of Bretherton et al. (1999). The lognormal modes of the modeled $N_{CCN}$ and $N_c$ are similar [log(230 cm$^{-3}$) and log(260 cm$^{-3}$), respectively], but the lognormal width of the optically retrieved $N_c$ (1.8) is a factor of about 3.6 wider than the lognormal width of $N_{CCN}$ (0.5; Figure 4a). Scatter plots of $N_{CCN}$ and $N_c$ versus LWP are shown in Figures 4c and 4d. The $N_{CCN}$ and $N_c$ distributions are limited above by a LWP$^{-1}$ power law, as observed for surface $N_{CCN}$ on additional research cruises at this location (de Szoeke et al., 2012).

While $N_{CCN}$ is weakly correlated with LWP, much of the widely distributed retrieved $N_c$ is related to LWP$^{-2}$, consistent with its optical dependence in equation (6). Scenes with average optical depth and high LWP (proportional to integrated water volume) must have low $N_c$, while scenes with very low LWP require more droplets in order to reach the same optical depth. The distribution of the retrieved $N_c$ is much wider than that of $N_{CCN}$ from the ship or in situ $N_c$ from aircraft in VOCALS (Snider et al., 2017). The retrieved $N_c$ is broadened by variations in $\tau_c$ that are uncorrelated with, and not representative of, contemporaneous variations in the overhead cloud LWP. The optically retrieved $N_c$ depends on the cube of $\tau_c$, which in turn depends on the average transmission ratio. Thus, our $N_c$ is sensitive to errors in LWP, $\tau_c$, and, to a lesser degree, $\Delta z$. Conversely, because $\tau_c \propto {N_c}^{1/3}$, we expect solar radiation to depend weakly on optically retrieved $N_c$. Despite these errors, the retrieved microphysical parameters are consistent by construction with surface solar radiation measurements, such that modeling radiative fluxes through clouds with the observed optical depths reproduces the fluxes observed at the surface.

Assuming LWC increases linearly within the cloud in this model, effective radius is 0 at cloud base and increases as the 1/3 power of height. Figure 4b shows the maximum $r_e$, that is, at cloud top, which follows the empirical relation $r_e(\mathrm{top}) = 16\ \mu\mathrm{m}\ [N_c/(100\ \mathrm{cm}^{-3})]^{-1/2}$. The $-1/2$ power is consistent with substituting LWP $\propto {N_c}^{-1/2}$ (from equation (6)) into the proportionality $r_e \propto (\mathrm{LWP}/N_c)^{1/3}$ between droplet radius and volume, assuming changes in cloud depth are small.

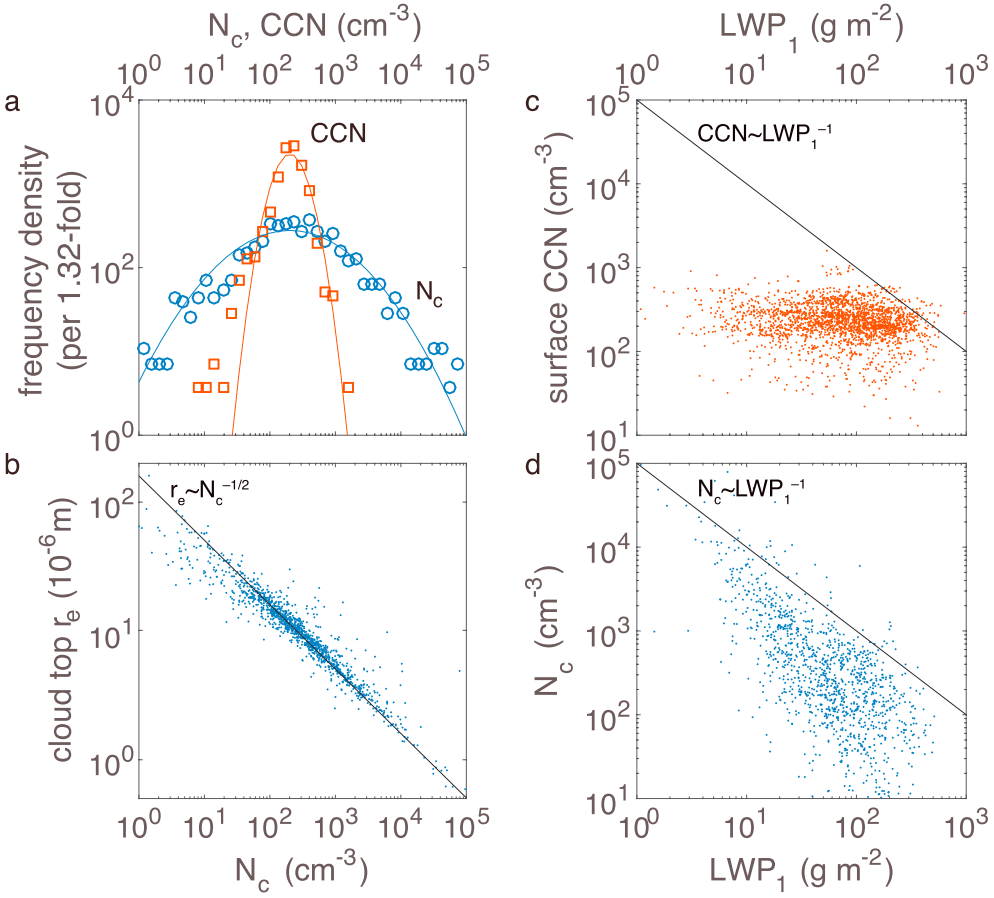


**Figure 4.** (a) Distributions of cloud droplet number concentration $N_c$ retrievals and surface-based CCN number concentration $N_{CCN}$ measurements, (b) retrieved effective radius at cloud top and $N_c$ (for reference the black line shows $r_e = 16\ \mu m \times (N_c/100\ cm^{-3})^{-1/2}$, (c) $N_{CCN}$ versus overcast liquid water path $LWP_1$ ($N_{CCN} \propto LWP_1^{-1}$, black line), and (d) $N_c$ versus $LWP_1$ ($N_c \propto LWP_1^{-1}$, black line). CCN = cloud condensation nuclei.

### 3.5. Logarithm of the Optical Model

The optical model relating the variables is converted to a linear equation by taking the natural logarithm of equation (6). The optical model becomes

$$3\log(\tau_c) = 3\log(\beta k) + 2\log(\mathrm{LWP}) + \log(\Delta z) + \log(N_c). \tag{7}$$

The variables inside the logarithms are found to be lognormally distributed, so the terms of (7) are Gaussian, and $\beta k$ is a constant. Subtracting the ensemble mean of the logarithms, denoted by the overbar, we define the anomaly variables $t$, $l$, $z$, and $n$,

$$t = 3\log(\tau_c) - \overline{3\log(\tau_c)}, \tag{8a}$$

$$l = 2\log(\mathrm{LWP}) - \overline{2\log(\mathrm{LWP})}, \tag{8b}$$

$$z = \log(\Delta z) - \overline{\log(\Delta z)}, \tag{8c}$$

$$n = \log(N_c) - \overline{\log(N_c)}. \tag{8d}$$

The model (7) for the anomalies of the logarithmic variables is then equivalent to the linear equation

$$t = l + z + n. \tag{9}$$

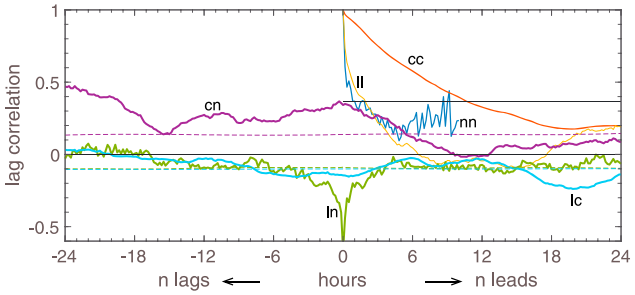


**Figure 5.** Lag correlations of *c* with *n*, *l* with *n*, and *l* with *c*. (*n* leads *c* and *t* for positive lag; *c* leads *l* for positive lag.) Correlations stronger than the dashed lines exceed 0 for two-tailed 0.95 statistical significance. (right) Lag autocorrelations of *c*, *n*, and *l*. Black line indicates 1/*e*.

## 4. Covariance Structure

The logarithms of $N_{CCN}$, LWP, and $N_c$ vary on vastly different time scales. The anomaly of the log of $N_{CCN}$, $c \equiv \log(N_{CCN}) - \overline{\log(N_{CCN})}$, is autocorrelated for nearly 11 hr (Figure 5). LWP, on which the $N_c$ retrieval strongly depends, is autocorrelated for 2 hr, while the retrieved $N_c$ is autocorrelated for only 40 min. Figure 5 shows the *n*, *l*, and *c* lag autocorrelations and where they cross $1/e \approx 0.368$ (black dotted line, right). The number of paired data for the autocorrelations depends on the lag. It is about 790 for *cn*; 1,120 for *ln*; and 2,220 for *lc*. The autocorrelation of each time series further reduces its effective degrees of freedom (Bretherton et al., 1999).

Figure 5 also shows lag correlations among *l*, *n*, and *c*. The contemporaneous anticorrelation between *l* and *n* is strong ($R = -0.6$) but only significant in a narrow window from −4- to +3-hr lag. The anomaly of the logarithm of $N_{CCN}$, *c*, leads *l* and *n*. The only symmetric lag correlation shown is between *l* and *n* (Figure 5, green line). CCN number concentration $N_{CCN}$ is correlated for the whole day prior and 5 hr following $N_c$ (Figure 5, purple). The CCN concentration *c* is anticorrelated to *l*, with *l* leading by ~4 hr. In the diurnal average, clouds are thinner in the afternoon, reaching a minimum at 17 local (de Szoeke et al., 2012). The diurnal $N_{CCN}$ maximum is at 21 local (not shown). The 24-hr time difference between the anticorrelation of *c* to *l* (Figure 5, cyan) at 20-hr lag ($R = -0.2$) and at −4 hr suggests it results from their diurnal cycles. The anticorrelation at 20-hr lag is slightly, but not significantly, greater than the anticorrelation at −4-hr lag, according to a Fischer-transformed *z* statistic.

Diurnal or synoptic variability of $N_{CCN}$ tends to modulate cloud microphysics (George & Wood, 2010; Painemal & Zuidema, 2010), affecting correlations at long lags. Diurnal decoupling and subsequent remixing between the surface layer and cloud (Burleyson et al., 2013; de Szoeke et al., 2012; Wyant et al., 1997) may modulate and delay the introduction of surface CCN to the cloud, as it does for sulfate aerosol (Yang et al., 2011). This diurnal cycle of decoupling might also explain the strong anticorrelation of LWP to $N_{CCN}$ at 20 hr.

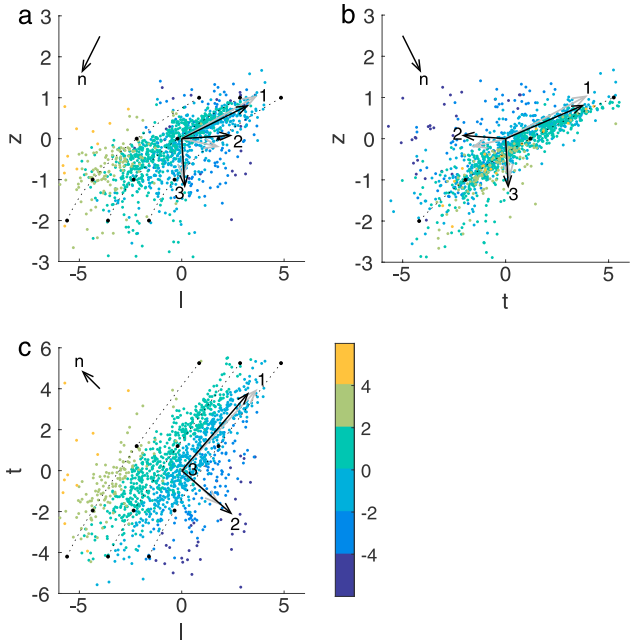


**Figure 6.** Scatter plot of observed $\tilde{l}$, $\tilde{z}$, $\tilde{t}$ projected onto the (a) *l*-*z*, (b) *z*-*t*, and (c) *l*-*t* planes. Colors of points show the estimated $\tilde{n}$. Because cloud thickness varies relatively little, the *z* axis is stretched by a factor of 2. Vectors labeled 1, 2, and 3 show the eigenvectors in descending order, scaled by their standard deviation. Vectors labeled *n* (upper left of each panel) show the direction of increasing *n* projected onto the plane of each pair of axes. A quadratic surface $t = -6 + 0.45(z + 4)^2$ that visually fits the data (Appendix B) is shown by $n = -1$, 1, and 3 contours (dashed). Black dots represent where $z = -2$, −1, 0, and 1 on this surface.

The joint distribution of the measurements of *l*, *z*, and *t* are shown projected onto the *l*-*z*, *t*-*z*, and *l*-*t* axes in the three scatter plots of Figure 6. The measurements span the *l*-*t* axes (Figure 6c). They are approximately aligned in a plane that tilts so that *z* increases with increasing *l* and *t*.

Table 1 shows the correlation coefficients (*R*, above the main diagonal) of the logarithmic variables *l*, *z*, *t*, and *n* and the fraction of variance (coefficient of determination $R^2$, below the main diagonal) explained by regression of each variable onto every other. Because these data are autocorrelated with a time scale slightly shorter than 2 hr, the number of degrees of freedom in this data set is conservatively reduced from 1,276 by a factor of 12 to 106. A priori correlations must have an absolute value exceeding 0.19 (for a two-tailed test) in order to be statistically significantly different from 0 at 0.95 confidence. All the correlations in Table 1 are thus significant except the one between $N_c$ and $\tau_c$. Nevertheless, the sign of this statistically insignificant correlation is consistent with the expectation that an optically thicker cloud has a greater $N_c$. LWP explains roughly 30% of the variability of $\Delta z$, and 40% of both $\tau_c$ and $N_c$. Cloud thickness $\Delta z$ explains nearly 50% of $\tau_c$ variability. Droplet number $N_c$ does not explain a significant fraction of $\tau_c$.

As expected, observed LWP and *l* and cloud depth *z* are related, with a correlation coefficient of 0.57. Cloud-microphysical interactions might lead to correlation or anticorrelation between $N_c$ and LWP (*n* and *l*). Deeper clouds (with more LWP) enhance coalescence and rainout of

**Table 1**
*Correlation Coefficients (R) Above the Main Diagonal, and Fraction of Covariance Explained ($R^2$, %) Below the Main Diagonal, of the Observed Logarithms of LWP $(\widetilde{l})$, Cloud Thickness $(\widetilde{z})$, Optical Depth $(\widetilde{t})$, and Retrieved $N_c$ $(\widetilde{n})$*

| | $\widetilde{l}$ | $\widetilde{z}$ | $\widetilde{t}$ | $\widetilde{n}$ |
|---|---|---|---|---|
| $\widetilde{l}$ | 1 | 0.57 | 0.65 | −0.67 |
| $\widetilde{z}$ | 32% | 1 | 0.69 | −0.31 |
| $\widetilde{t}$ | 42% | 47% | 1 | *0.10* |
| $\widetilde{n}$ | 44% | 10% | *1%* | 1 |

*Note.* Two-tailed 95% significance requires $R < 0.19$, assuming 107 degrees of freedom. The statistically insignificant correlation between $\widetilde{t}$ and $\widetilde{n}$ is italicized.

cloud droplets, over time reducing $N_c$ (Hudson et al., 2015; Yum & Hudson, 2002). This effect would result in $l$ (and $z$) anticorrelated with $n$. We do in fact observe negative correlation coefficients $\widetilde{R}_{ln} = -0.67$ and $\widetilde{R}_{zn} = -0.31$.

This could be evidence for cloud-microphysical interaction. We first consider whether sampling error is responsible for the large retrieved microphysical ($N_c$) variability. One source of error is that the hemispheric downwelling shortwave radiation, from which we derive cloud optical depth, may not be representative of LWP estimated from a microwave field of view of 2.5°, and cloud thickness estimated from ~1° radar and ceilometer fields of view. Even the 10-min averages do not necessarily yield a representative ensemble of the clouds. The retrieval requires low $N_c$ in order to match moderate $\tau_c$ when LWP and $\Delta z$ are high. It is possible that both cloud microphysics and sampling error reduce the correlation between $l$ and $t$, but all of this variability projects onto the retrieved $N_c$.

We develop a method for analyzing the covariance structure that corrects the covariance matrix for the correlated errors. The observations $(\widetilde{l}, \widetilde{z}, \widetilde{t})$ are the sum of the true variables ($l$, $z$, $t$) and the error ($l'$, $z'$, $t'$),

$$\left(\widetilde{l}, \widetilde{z}, \widetilde{t}\right) = (l, z, t) + (l', z', t').$$

We assume that the observational errors are random and uncorrelated with any of the true variables. The errors can be correlated among themselves, however. The covariance matrices of the observations and the errors are shown in Table 2.

We estimate the error covariance matrix from the lag covariances (Figure 7). All the covariances have maxima at zero lag. We attribute most of the variance of these maxima to sampling noise that is uncorrelated with physical variability. The decrease between the zero-lag and the one-lag (10 min) autocovariances $\overline{l'l'}$, $\overline{z'z'}$, and $\overline{t't'}$, is greater than the decrease at longer lags. The lag autocovariance continues to decrease for longer lags, probably because of the finite timescales of boundary layer overturns and mesoscale cloud structure. We interpret the level that the maximum at zero lag exceeds the one-lag autocovariance (10 min; Figure 7, solid lines) as the error covariance. It is possible that this overestimates the error by counting some of the true variability at zero lag as error. We estimate the off-diagonal covariances of $\mathbf{C}'$, $\overline{l'z'}$, $\overline{l't'}$, and $\overline{z't'}$, from the lagged cross-covariances, as for the autocovariances (Table 2, right). Compared to the single isolated maximum point in contemporaneous autocovariance, the maxima in the lagged cross-covariances are ±20–30 min wide (Figure 7, open circles). Conservatively, we compute the error covariances $\overline{l'z'}$, $\overline{l't'}$, and $\overline{z't'}$ as the peak covariance at lag 0 minus the covariance at the "ankle" where the lag covariance starts to decrease more slowly. For covariances $\overline{l'z'}$ and $\overline{l't'}$ the ankle is at 30 min; for $\overline{z't'}$ the ankle is at 20 min.

Since the observed covariance matrix $\widetilde{\mathbf{C}}$ is the sum of the covariance matrix of the true variables $\mathbf{C}$ and that of the errors $\mathbf{C}'$, the true covariance matrix is

$$\mathbf{C} = \widetilde{\mathbf{C}} - \mathbf{C}'. \tag{10}$$

The eigenvectors of the true covariance matrix are the true empirical orthogonal modes of variability in the VOCALS cloud data set. The eigenvectors $\boldsymbol{v}_1$, $\boldsymbol{v}_2$, and $\boldsymbol{v}_3$ are displayed as columns (i.e., [$l$, $z$, $t$] components) in Table 3. The sign of each eigenvector is arbitrary. Scaled by the square root of their eigenvalue, so they are proportional to the standard deviation explained by each mode, the eigenvectors are projected onto the axes of Figure 6. The middle three columns of Table 3 show the eigenvectors of the error covariance $\mathbf{C}'$. We also computed the eigenvectors of the observed covariance matrix $\widetilde{\mathbf{C}}$, (Table 3, right) without subtracting the error covariance (Figure 6, gray vectors). Though the total variance (fourth row, Table 3) is reduced by 33% by subtracting the error covariance, the effect of the error covariance on the eigenvectors is minimal. The eigenvectors of the true covariance matrix are very similar to the

**Table 2**
*Covariances of Observed $\left(\widetilde{l}, \widetilde{z}, \widetilde{t}\right)$ and Retrieved $\widetilde{n}$, and Random Errors ($l'$, $z'$, $t'$)*

| | $\widetilde{l}$ | $\widetilde{z}$ | $\widetilde{t}$ | $\widetilde{n}$ | | $l'$ | $z'$ | $t'$ |
|---|---|---|---|---|---|---|---|---|
| $\widetilde{l}$ | 4.30 | 0.86 | 2.93 | −2.54 | $l'$ | 1.13 | 0.18 | 1.1 |
| $\widetilde{z}$ | | 0.54 | 1.09 | −0.42 | $z'$ | | 0.15 | 0.38 |
| $\widetilde{t}$ | | | 4.71 | *0.41* | $t'$ | | | 1.41 |
| $\widetilde{n}$ | | | | 3.37 | | | | |

*Note.* The italicized covariance is statistically insignificant. Symmetric covariances are not shown below the main diagonal.

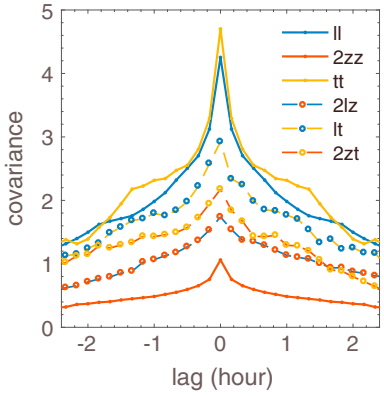


**Figure 7.** Lag autocovariance for observed variables $\widetilde{l}$, $\widetilde{z}$, and $\widetilde{t}$; and their cross covariances. Variances and covariances with $\widetilde{z}$ have been multiplied by 2.

eigenvectors of the observed covariance matrix (Table 3). For this reason, we are satisfied that the error covariances are not grossly overestimated, and the results are not sensitive to the error covariance matrix.

The *l*, *t*, and *z* components of each eigenvector give its projection onto the logarithm of cloud droplet number $n = t - l - z$. Table 3 shows the empirical (orthogonal) eigenvectors in order of the amount of variance they explain in *l*, *t*, *z* space. By construction of the optical model, these modes explain variations consistent with observed changes in optical depth. The variance explained (the eigenvalue) by the first eigenvector $\boldsymbol{v}_1$ is 2.4 times that of the second $\boldsymbol{v}_2$, but the LWP (*l*) and $\tau_c$ (*t*) components of $\boldsymbol{v}_1$ cancel out, having negligible effect on $N_c$ (*n*). The first eigenvector $\boldsymbol{v}_1$ describes almost all *macrophysical* (LWP and cloud thickness) variability that is statistically independent of microphysical ($N_c$) variability. The second eigenvector $\boldsymbol{v}_2$ explains most of the empirical *microphysical* variability of *n*, about 4 times as much of the amplitude of *n* as the third eigenvector. Empirically, the macrophysical mode explains $\tau_c$ increasing with LWP. The microphysical mode explains when optical depth increases while LWP decreases—which implies an increase in $N_c$. The third eigenvector is small, representing small residual variance of cloud thickness (*z*), and henceforth, we neglect it.

Truncation of the third eigenvector collapses the observed variability onto the plane of $\boldsymbol{v}_1$, $\boldsymbol{v}_2$, that is determined mostly by LWP and $\tau_c$. This plane describes the empirical variability. The plane of variability is a regression model for *z* on *l* and *t* that minimizes the distance of the realizations normal to the plane in a least squares sense. In the next section, we compute the sensitivities, especially of LWP to $N_c$, from the slope of this plane in *l*, *z*, *t* (and *n*) space.

## 5. Sensitivity of Macrophysical to Microphysical Variables

We determine the empirical sensitivity dlog($N_c$)/dlog(LWP) of droplet number concentration $N_c$ to LWP from d*n*/d*l*, the directional derivative in the plane of variability described by the eigenvectors $\boldsymbol{v}_1$ and $\boldsymbol{v}_2$ of the true covariance matrix $\mathbf{C}$. The derivative depends upon the projections of the gradients ∇n and ∇l into the plane of variability. Also, it depends on the arbitrary direction within the plane at which it is measured. We estimate two empirical sensitivities. First, the derivative is computed in the direction of the projection of the differentiating variable onto the plane, for example, for the derivative of *n* with respect to *l*,

$$(\mathrm{d}n/\mathrm{d}l)_l = (\nabla_e n \cdot \nabla_e l)/(\nabla_e l \cdot \nabla_e l), \tag{11}$$

where $\nabla_e n$ and $\nabla_e l$ are the projections of the gradients of *n* and *l* in the plane of the eigenvectors $\boldsymbol{v}_1$ and $\boldsymbol{v}_2$,

$$\nabla_e n = (\nabla n \cdot \boldsymbol{v}_1)\boldsymbol{v}_1 + (\nabla n \cdot \boldsymbol{v}_2)\boldsymbol{v}_2.$$

**Table 3**
*Eigenvectors of Covariance Matrices of the Data l, z, t: The True Covariance Matrix* $\mathbf{C}$*, the Error Covariance* $\mathbf{C}'$*, and the Observed Covariance* $\widetilde{\mathbf{C}}=\mathbf{C}+\mathbf{C}'$

| | True eigenvectors $\mathbf{C}$ | | | Error $\mathbf{C}'$ | | | Observed $\widetilde{\mathbf{C}}$ | | |
|---|---|---|---|---|---|---|---|---|---|
| | $\boldsymbol{v}_1$ | $\boldsymbol{v}_2$ | $\boldsymbol{v}_3$ | $\boldsymbol{v}_1$ | $\boldsymbol{v}_2$ | $\boldsymbol{v}_3$ | $\boldsymbol{v}_1$ | $\boldsymbol{v}_2$ | $\boldsymbol{v}_3$ |
| *l* | 0.64 | 0.76 | 0.12 | 0.64 | 0.68 | 0.34 | 0.67 | 0.74 | 0.07 |
| *z* | 0.16 | 0.02 | −0.99 | 0.17 | −0.57 | 0.80 | 0.19 | −0.08 | −0.98 |
| *t* | 0.75 | −0.65 | 0.11 | 0.75 | −0.46 | −0.48 | 0.72 | −0.67 | 0.19 |
| Variance | 6.56 | 2.70 | 0.38 | 2.45 | 0.24 | 0.00 | 7.70 | 1.58 | 0.26 |
| Frac. variance | 0.68 | 0.28 | 0.04 | 0.91 | 0.09 | 0.00 | 0.81 | 0.17 | 0.03 |
| Amplitude | 2.56 | 1.64 | 0.61 | 1.57 | 0.49 | 0.04 | 2.78 | 1.26 | 0.51 |
| Proj. onto *n* | −0.06 | −1.44 | 0.97 | −0.07 | −0.57 | −1.63 | −0.14 | −1.33 | 1.10 |
| *n* amplitude | −0.14 | −2.36 | 0.59 | −0.11 | −0.28 | −0.06 | −0.38 | −1.67 | 0.56 |

*Note.* The signs of the eigenvectors are arbitrary. Variance (eigenvalue), fraction of total variance $R^2$, and amplitude (standard deviation) explained by each eigenvector; and their projection onto cloud droplet number concentration *n*.

**Table 4**
*Empirical Power Law Sensitivities Deduced From Directional Derivatives d(log p)/d(log q) Evaluated on the Empirical Plane of Variability Described by the Two Eigenvectors $\mathbf{v}_1$, $\mathbf{v}_2$ of the Covariance Matrix*

| | | | q | | | |
|---|---|---|---|---|---|---|
| d(log p)/d(log q) | | | LWP | $\Delta z$ | $\tau_c$ | $N_c$ |
| \|\| to q | p | LWP | 1 | 2.30 | −0.02 | −0.27 |
| | | $\Delta z$ | 0.25 | 1 | 0.32 | −0.02 |
| | | $\tau_c$ | −0.01 | 1.31 | 1 | 0.15 |
| | | $N_c$ | −2.28 | −1.68 | 2.72 | 1 |
| Maximum | | LWP | 1 | 4.02 | *−112* | −0.44 |
| | | $\Delta z$ | 0.43 | 1 | 0.76 | *−0.60* |
| | | $\tau_c$ | *−50* | 3.15 | 1 | 0.37 |
| | | $N_c$ | −3.68 | *−46* | 6.89 | 1 |

*Note.* Derivatives are computed two ways described in the text: In the direction of the plane parallel to the differentiating variable q (||, equation (11)), and in the direction in the plane that the derivative is maximum (12). Italics show poorly posed maximum derivatives. LWP = liquid water path.

A second sensitivity is computed from the maximum directional derivative, that is, taken in the direction within the plane of variability that maximizes it. It is given by

$$(\mathrm{d}n/\mathrm{d}l)_{\max} = (\nabla_e n \cdot \nabla_e n)/(\nabla_e n \cdot \nabla_e l). \quad (12)$$

The maximum directional derivative $(\mathrm{d}n/\mathrm{d}l)_{\max}$ of equation (12) is not well posed when the angle between the projections of the differentiated and differentiating variables are nearly orthogonal. Both empirical sensitivities (11) and (12) are negative if the angle between projections of the gradients $\nabla_e n$ and $\nabla_e l$ is more than 90°.

From (11) and (8a) to (8d) we calculate

$$(\mathrm{d}\log N_c/\mathrm{d}\log \mathrm{LWP})_{\mathrm{LWP}} = 2(\mathrm{d}n/\mathrm{d}l) = -2.3.$$

The sensitivity is slightly stronger in the plane of variability of the true covariance matrix than it is for the observed covariance before removing the error covariance (−2.2). We also test the robustness of the sensitivity by computing it on several smaller subsets of the data: divided by morning and afternoon, divided by longitude, and divided into the upper and lower halves of the distributions of $\widetilde{l}$, $\widetilde{t}$, and $\widetilde{n}$, respectively. The standard deviation of these 10 different ways of computing the sensitivity is 0.19 (9%). The sensitivity is −2.3 for observations west of 80°W and −2.0 for observations east of 80°W. Thus, the sensitivity is robust to dividing the data set.

We similarly calculate the sensitivities d(log *p*)/d(log *q*) within the plane of variability among all the variables LWP, $\Delta z$, $\tau_c$, and $N_c$ in Table 4. The sensitivities of $N_c$ to LWP and to $\tau_c$ (2.7) are strong because LWP and $\tau_c$ project strongly onto the plane of variability and because sensitivities to LWP and $\tau_c$ gain factors of 2 and 3 from their quadratic and cubic dependence. Inversely, the sensitivity of $\tau_c$ to droplet number $(\mathrm{d}\log(\tau_c)/\mathrm{d}\log(N_c))_{N_c} = (\mathrm{d}t/\mathrm{d}n)_n/3 = 0.15$ is quite small. The sensitivities of optical depth to LWP, and vice versa, are negligible because LWP and optical depth are nearly orthogonal in the empirical plane of variability.

Taking the derivative in the direction that maximizes it within the plane of variability (12) roughly doubles most of the derivatives, with $(\mathrm{d}\log N_c/\mathrm{d}\log \mathrm{LWP})_{\max} = -3.7$, which is 61% greater than $(\mathrm{d}\log N_c/\mathrm{d}\log \mathrm{LWP})_{\mathrm{LWP}}$. The very small "maximum" empirical sensitivity between $\Delta z$ and $N_c$, and the very large maximum sensitivity between LWP and $\tau_c$, are not reliable because the projections of these gradients onto the plane of variability are nearly mutually orthogonal. (The angle between $\nabla_e n$ and $\nabla_e z$ is 101° and between $\nabla_e t$ and $\nabla_e l$ is 91°.) Cloud thickness $\Delta z$ variability is small and nearly orthogonal to the plane of variability.

### 5.1. Influence of Drizzle

The number and size distribution of the cloud droplets influences the collision-coalescence process by which drizzle forms. Coalescence and drizzle reduce the number of droplets and CCN (Hudson et al., 2015), and drizzle removes water from the cloud. We investigate how drizzle influences microphysical-macrophysical cloud interactions with lag covariances of logarithms of radar area-averaged rain rate, LWP, $N_c$, and $N_{CCN}$ (Figure 8). Rain rate is strongly autocorrelated at lags of hours to 1 day, with a strong diurnal cycle. The covariance operation with the area-average rain rate filters out uncorrelated high-frequency noise from the narrower field-of-view retrievals. Rain has a strong diurnal cycle itself, so regressions against it emphasize the diurnal cycle.

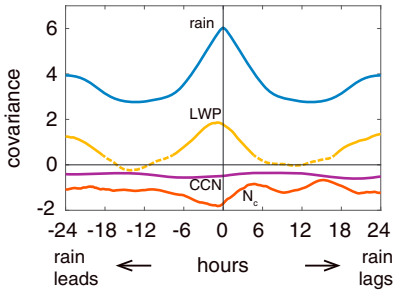


**Figure 8.** Covariances of the logarithms of rain with LWP, $N_{CCN}$, and $N_c$. Dashed line (LWP-rain covariance) is not significantly different from 0; all other covariances are significant. CCN = cloud condensation nuclei; LWP = liquid water path.

The diurnal cycle of drizzle and LWP are similar. Both are forced by the diurnal cycle of radiative divergence, which drives turbulence, cloud-top entrainment, and coupling between the subcloud surface layer and the cloud. The LWP peak lags the drizzle peak by 2 hr. Cloud droplet number $N_c$ and surface CCN concentrations $N_{CCN}$ are negatively correlated with drizzle at all lags, perhaps reflecting that the ship

traversed a large-scale longitudinal gradient with deeper boundary layers, more drizzle, and cleaner aerosol loading further offshore.

Rain rate lag covariance with $N_c$ suggests that $N_c$ responds to drizzle on hourly time scales. Cloud droplet number $N_c$ is most negatively correlated 1 hr after drizzle. The most negative covariance with $N_c$ lags the drizzle peak autocovariance by 1 hr. This lag is consistent with drizzle reducing $N_c$ by collision-coalescence. LWP is most correlated with drizzle 1–2 hr following drizzle. Anticorrelation of LWP to $N_c$, in relation to drizzle, means that the microphysical cloud lifetime effect, whereby greater $N_c$ requires greater LWP to generate drizzle, does not govern the temporal coevolution of $N_c$, LWP, and drizzle for these clouds. The LWP maximum following the drizzle means liquid water removal by drizzle is canceled by an even stronger positive source of condensate. The source or sink of LWP that can be attributed to microphysical effects, or even drizzle, appears to be minor compared to other sustained sources, such as entrainment and decoupling. These are forced by larger-scale phenomena such as the diurnal cycle.

## 6. Conclusions

Droplet number concentration $N_c$ is retrieved with a large logarithmic standard deviation ($\sigma_n = 1.8$) in order to explain large observed standard deviation of the cube of cloud optical depth ($\sigma_t = 2.2$) that is not correlated to LWP ($\sigma_l = 2.1$). Droplet number concentration $N_c$ is significantly anticorrelated to LWP ($R_{nl} = -0.67$). This corroborates previous anticorrelations $R = -0.27$ (Painemal & Zuidema, 2010) and, though statistically insignificant, $R = -0.33$ (Twohy et al., 2005). These negative correlations are contrary to the correlation found for 10 VOCALS research flights closer to shore (20°S, 72°W; Zheng et al., 2010). The covariability of $\tau_c$ with LWP is much stronger than the statistically insignificant $\tau_c$ cloud optical depth variability with $N_c$.

Almost all of the macrophysical-microphysical variability of the southeast Pacific stratocumulus clouds observed during VOCALS (September–October 2008; 20°S, 75°–85°W) is described by two statistically independent modes of cloud optical depth, LWP, and cloud thickness. A macrophysical mode explains 68% of the multidimensional variance of $l$, $t$, and $z$, which are the logarithms of $\tau_c$, LWP, and cloud thickness $\Delta z$, scaled by their respective powers in the optical model for droplet number concentration. In the macrophysical mode, cloud optical depth, LWP, and to a lesser degree $\Delta z$ increase together, such that they have a negligible effect on the retrieved $N_c$. The second mode dominates the microphysical variability. It explains 28% of the total variance of $l$, $t$, $z$ and 100 times more of the $N_c$ variance than the first mode. The microphysical mode describes LWP that decreases for greater $N_c$. This is opposite of the sensitivity hypothesized by the cloud lifetime aerosol indirect effect (Albrecht, 1989).

These two modes describe a plane of empirical variability. We estimate sensitivities among the variables studied as directional derivatives of these variables with respect to one another in this plane of variability. Droplet number is strongly anticorrelated to LWP ($R = -0.67$), with a sensitivity of $(\mathrm{d}\log(N_c)/\mathrm{d}\log(\mathrm{LWP}))_{Nc} = -2.3$. Observations of LWP and $N_c$ were also anticorrelated in DYCOMS-II (Twohy et al., 2005) and in satellite observations of the VOCALS southeastern tropical Pacific (Painemal & Zuidema, 2010). Those and the present study imply that the macrophysical variability of clouds exerts a strong influence on the microphysics. While we cannot ascribe cause and effect from these statistical correlations, the negative correlation is consistent with $N_c$ being very sensitive to LWP.

The weak negative empirical sensitivity of LWP to $N_c$ ($-0.27$) is inconsistent with greater $N_c$ enhancing LWP by suppressing precipitation (Albrecht, 1989). Entrainment drying or drizzle processes may overwhelm this cloud lifetime effect and explain the negative correlation. Entrainment drying has been found to reduce LWP more effectively for greater $N_c$ (Ackerman et al., 2004; Jiang et al., 2002) in LES of stratocumulus during daylight or when air entrained from above the inversion is dry. The VOCALS stratocumulus clouds are capped above the inversion by low specific humidity (1 g/kg; de Szoeke et al., 2012) and respond to the diurnal solar cycle (Burleyson et al., 2013; Painemal et al., 2013).

Lower $N_c$ could also result from collection of cloud droplets by drizzle from clouds with greater LWP (Wood et al., 2012). Drizzle starts when cloud droplets reach a critical size for coalescence (e.g., Gerber, 1996; Hudson & Yum, 2001). For vertically uniform $N_c$, the droplet size increases with height within the cloud. As a result, drizzle increases with cloud thickness (Yum & Hudson, 2002). The southeastern Pacific stratocumulus clouds in this study are 200–400 m thick (de Szoeke et al., 2012). They last for days, with reduced cloud fraction in the

afternoon. If drizzle is already active within the clouds, even if it does not reach the surface, then increasing $N_c$ does not delay the onset of drizzle, and its effect may be insufficient to arrest the autoconversion of cloud to drizzle. If the southeastern Pacific stratocumulus clouds drizzle enough, and the clouds last for days in any case, then increasing $N_c$ cannot extend the cloud lifetime. These clouds are indeed actively drizzling most of the time. Radar reflectivity at least 25 m below cloud base indicates drizzle leaving cloud base in 72% of the clouds detected by the ceilometer. Of these, 67% have fall velocity exceeding 0.25 m/s.

Surface CCN concentration $N_{CCN}$ is weakly but significantly correlated to $N_c$ for the whole day leading $N_c$, implying synoptic forcing of $N_{CCN}$ and a slow response of the clouds to $N_{CCN}$. Surface CCN is anticorrelated with LWP at most lags. Positive LWP leads negative $N_{CCN}$ by 4 hr in the mean diurnal cycle (not shown), explaining the stronger anticorrelation of LWP and $N_{CCN}$ at −4 and +20 hr. The difference in the strength of the anticorrelation of $N_{CCN}$ and LWP at −4 and +20 hr is not significant.

Time lag correlations of area-averaged radar rain rate with LWP and $N_c$ retrievals indicate that LWP and drizzle vary strongly over the diurnal cycle. Rain is correlated with LWP and anticorrelated with $N_c$. LWP continues to increase and $N_c$ to decrease 1–2 hr past the peak drizzle, suggesting that sources of moisture external to the cloud have a dominant influence on the LWP and drizzle, and drizzle dominates the variability of $N_c$, rather than the converse.

The empirical sensitivities and correlations measured here are an emergent constraint for evaluating cloud-aerosol interactions in models, from LES to climate models. Different fields of view among remote sensing instruments lead to sampling errors in remotely sensed cloud measurements. Observations of cloud macrophysical-microphysical interactions depend on estimates of these sampling errors. We made assumptions to account for these correlated errors in our analysis. Subsequent deployments of suites of sensors may improve on these estimates by endeavors to sample more precisely the same volume of cloud or to better quantify the sampling error in a given suite of observations.

## Appendix A: Comparison With a Previous Microphysical Retrieval

Dong et al. (1998; hereafter D98) optimized the cloud droplet effective radius $r_e$ to match observed surface downwelling solar radiation with a radiative transfer scheme. Their statistical fit provides an empirical formula for effective radius $r_e$ (in units of $10^{-6}$ m) as a function of cloud transmission ratio $\gamma$, LWP (specified in units of 100 g /m$^2$), and cosine of solar zenith angle $\mu_0$:

$$r_e = -2.07 + 2.49(\mathrm{LWP}) + 10.25\gamma - 0.25\mu_0 + 20.28\gamma(\mathrm{LWP}) - 3.14\mu_0(\mathrm{LWP}). \quad \text{(A1)}$$

Radiative transfer calculations using this effective radius reproduce measured surface radiation very accurately for the VOCALS clouds (Verlinden & de Szoeke, 2018). When providing $r_e$ and LWP to the radiative transfer model, the integrated optical depth is insensitive to the vertical distribution of liquid water in the cloud, either due to the cloud depth or due to the LWC rate of increase with height in the cloud. In order to retrieve radiative divergence *within* the cloud, Verlinden and de Szoeke (2018) assume vertically uniform $N_c$, and vary $r_e$ with height to match a LWC profile that increases linearly from cloud base. The $N_c$ retrieval from (6) is sensitive to cloud thickness $\Delta z$, yet the product of $N_c(\Delta z)$ is not.

We solve (6) for the $N_c$ implied by D98 from the cloud optical depth,

$$\tau_c = 3Q_e\,\mathrm{LWP}/(4\rho_w r_e), \quad \text{(A2)}$$

using the $r_e$ from (A1). Figure A1 compares the cloud optical depth retrieved directly from transmission ratios with those from the D98 regression. The variable $(N_c\,\Delta z)^{1/3}$ on the $x$ axis indicates the effect of $\tau_c$ on the microphysics. The different optical depth retrievals share the same LWP. The straight lines connecting the two retrievals have slope $\tau_c/(N_c\,\Delta z)^{1/3} \propto \mathrm{LWP}^{2/3}$. After removing negative D98 optical depths,

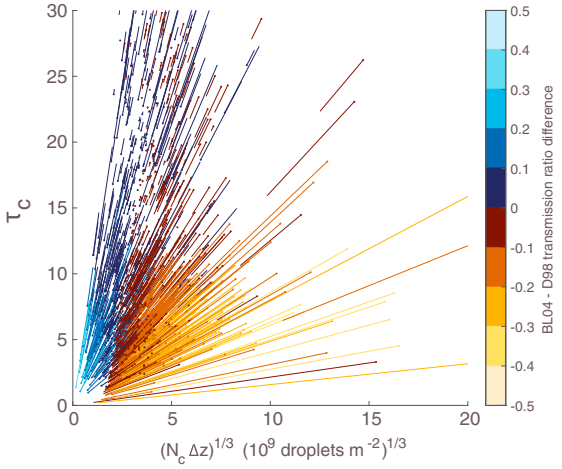


**Figure A1.** Optical depth retrieval $\tau_c$ (dots) compared to the Dong et al. (1998; D98) regression of $\tau_c$ on transmission ratio, cosine of zenith angle, and liquid water path (LWP; end of lines without dots). Colors denote the difference between our transmission ratios (adapted from Barnard & Long, 2004; BL04) and those predicted by D98. The slope of the line connecting the two retrievals $\tau_c/(N_c\,\Delta z)^{1/3}$ is proportional to LWP$^{2/3}$.

our mean optical depth is 0.4 greater than the mean of D98; 60% of our direct optical depths are greater than those from D98. The root-mean-square difference is 2.5, and the correlation of the two optical depth retrievals is $R = 0.96$.

In contrast to our $\tau_c$ retrieval, the empirical cloud optical depth of D98 also depends on LWP. The second and last terms of (A1) are small and approximately cancel because $\mu_0$ is at most one. Under these simplifications, partial differentiation of the D98 regression $\partial\tau_{c,D98}/\partial$(LWP) becomes negative for $\gamma < \sim 0.2$. While it reproduces the observed surface solar radiation well, we have no way to evaluate whether the D98 regression is physical in the various ranges of the observed parameters. We retain our $\tau_c$ that has no empirical LWP dependence for statistics used to infer microphysical-macrophysical interactions.

## Appendix B: Elaborating the Empirical *l*, *z*, *t* Distribution

The variability of *l*, *z*, and *t* is well described by the plane of the two eigenvectors $\boldsymbol{v}_1$ and $\boldsymbol{v}_2$. A close look at the scatter plots (Figure 6) reveals that the joint distribution of *t* and *z* (Figure 6b) appears to be arranged in a slightly concave-down (toward negative *z*) curve, with a quadratic dependence

$$t \approx -6 + 0.45(z+4)^2 \tag{B1}$$

of *t* on *z* (denoted by the hairline), independent of *l*. The change in slope of the quadratic curve implies that cloud optical depth is more sensitive to cloud thickness for thicker clouds, that is, the proportionality $\tau_c \propto (\Delta z)^b$ has a greater exponent *b*. Differentiating the empirical *z*-*t* curve, (B1) gives an exponent $b = 0.9$ for $\Delta z = 70$ m, and $b = 1.5$ for $\Delta z = 520$ m.

The distribution tilts ever so slightly to higher *z* for lower *n*. Outliers with very low *n* are found for very thick clouds. We have low confidence in the curve fit with logarithm of cloud thickness *z* significantly above the curve described by (B1) for extremely clean $N_c$. The 41 outliers with $N_c < 3.6$ cm$^{-3}$ (dark blue) and unusually thick clouds, might be explained by overestimated cloud thickness, perhaps from the ceilometer detecting the lower bases of cumulus clouds under stratocumulus.

**Acknowledgments**
We thank J. Hudson and two anonymous reviewers for their insightful perspectives and comments on the manuscript, P. Zuidema for helpful comments and for providing the VOCALS liquid water path (LWP) data, and S. Yuter for the radar rain rate data. The surface-based aerosol size and chemistry data are available since 2009 at NOAA PMEL (https://saga.pmel.noaa.gov/data/nsd_info_dnld.php?cruise=VOCALS), and modeled CCN concentration data are available at in the Tropical Southeast Pacific Synthesis data set (http://people.oregonstate.edu/~deszoeks/synthesis.html). The PSD ship data for research cruises to the Woods Hole Ocean Reference Station are available in the Tropical Southeast Pacific Synthesis data set. This work was funded by National Science Foundation (NSF) grants 1619903 and 1600109, US Department of Energy grant DE-SC0006994, Office of Naval Research (ONR) grant N00014-16-1-3094, and the National Oceanic and Atmospheric Administration Climate Program Office Climate Variability and Predictability (NOAA CVP) grant NA15OAR4310242.

## References

Ackerman, A. S., Kirkpatrick, M. P., Stevens, D. E., & Toon, O. B. (2004). The impact of humidity above stratiform clouds on indirect aerosol climate forcing. *Nature*, *432*(7020), 1014–1017. https://doi.org/10.1038/nature03174

Albrecht, B. A. (1989). Aerosols, cloud microphysics, and fractional cloudiness. *Science*, *245*(4923), 1227–1230. https://doi.org/10.1126/science.245.4923.1227

Allen, G., Coe, H., Clarke, A., Bretherton, C., Wood, R., Abel, S. J., et al. (2011). South East Pacific atmospheric composition and variability sampled along 20°S during VOCALS-REx. *Atmospheric Chemistry and Physics*, *11*(11), 5237–5262. https://doi.org/10.5194/acp-11-5237-2011

Barnard, J. C., & Long, C. N. (2004). A simple empirical equation to calculate cloud optical thickness using shortwave broadband measurements. *Journal of Applied Meteorology*, *43*(7), 1057–1066. https://doi.org/10.1175/1520-0450(2004)043<1057:ASEETC>2.0.CO;2

Bretherton, C., Blossey, P., & Uchida, J. (2007). Cloud droplet sedimentation, entrainment efficiency, and subtropical stratocumulus albedo. *Geophysical Research Letters*, *34*, L03813. https://doi.org/10.1029/2006GL027648

Bretherton, C. S., Widmann, M., Dymnikov, V. P., Wallace, J. M., & Bladé, I. (1999). The effective number of spatial degrees of freedom of a time-varying field. *Journal of Climate*, *12*(7), 1990–2009. https://doi.org/10.1175/1520-0442(1999)012<1990:TENOSD>2.0.CO;2

Burleyson, C. D., de Szoeke, S. P., Yuter, S. E., Wilbanks, M., & Brewer, W. A. (2013). Ship-based observations of the diurnal cycle of Southeast Pacific marine stratocumulus clouds and precipitation. *Journal of the Atmospheric Sciences*, *70*(12), 3876–3894. https://doi.org/10.1175/JAS-D-13-01.1

Carslaw, K. S., Lee, L. A., Reddington, C. L., Pringle, K. J., Rap, A., Forster, P. M., et al. (2013). Large contribution of natural aerosols to uncertainty in indirect forcing. *Nature*, *503*(7474), 12674. https://doi.org/10.1038/nature12674

de Szoeke, S. P., Fairall, C. W., Wolfe, D. E., Bariteau, L., & Zuidema, P. (2010). Surface flux observations on the southeastern tropical Pacific Ocean and attribution of SST errors in coupled ocean–atmosphere models. *Journal of Climate*, *23*(15), 4152–4174. https://doi.org/10.1175/2010JCLI3411.1

de Szoeke, S. P., Yuter, S., Mechem, D., Fairall, C. W., Burleyson, C. D., & Zuidema, P. (2012). Observations of stratocumulus clouds and their effect on the eastern Pacific surface heat budget along 20°S. *Journal of Climate*, *25*(24), 8542–8567. https://doi.org/10.1175/JCLI-D-11-00618.1

Dong, X., Ackerman, T. P., & Clothiaux, E. E. (1998). Parameterizations of the microphysical and shortwave radiative properties of boundary layer stratus from ground-based measurements. *Journal of Geophysical Research*, *103*(D24), 31,681–31,693. https://doi.org/10.1029/1998jd200047

Dong, X., Ackerman, T. P., Clothiaux, E. E., Pilewskie, P., & Han, Y. (1997). Microphysical and radiative properties of boundary layer stratiform clouds deduced from ground-based measurements. *Journal of Geophysical Research*, *102*(D20), 23,829–23,843. https://doi.org/10.1029/97jd02119

Ferek, R. J., Garrett, T., Hobbs, P. V., Strader, S., Johnson, D., Taylor, J. P., et al. (2000). Drizzle suppression in ship tracks. *Journal of the Atmospheric Sciences*, *57*(16), 2707–2728. https://doi.org/10.1175/1520-0469(2000)057<2707:DSIST>2.0.CO;2

George, R. C., & Wood, R. (2010). Subseasonal variability of low cloud radiative properties over the Southeast Pacific Ocean. *Atmospheric Chemistry and Physics*, *10*(8), 4047–4063. https://doi.org/10.5194/acp-10-4047-2010

Gerber, H. (1996). Microphysics of marine stratocumulus clouds with two drizzle modes. *Journal of the Atmospheric Sciences*, *53*(12), 1649–1662. https://doi.org/10.1175/1520-0469(1996)053<1649:MOMSCW>2.0.CO;2

Ghan, S., Wang, M., Zhang, S., Ferrachat, S., Gettelman, A., Griesfeller, J., et al. (2016). Challenges in constraining anthropogenic aerosol effects on cloud radiative forcing using present-day spatiotemporal variability. *Proceedings of the National Academy of Sciences of the United States of America*, *113*(21), 5804–5811. https://doi.org/10.1073/pnas.1514036113

Gryspeerdt, E., Quaas, J., & Bellouin, N. (2016). Constraining the aerosol influence on cloud fraction. *Journal of Geophysical Research: Atmospheres*, *121*, 3566–3583. https://doi.org/10.1002/2015JD023744

Hawkins, L. N., Russell, L. M., Covert, D. S., Quinn, P. K., & Bates, T. S. (2010). Carboxylic acids, sulfates, and organosulfates in processed continental organic aerosol over the Southeast Pacific Ocean during VOCALS-REx 2008. *Journal of Geophysical Research*, *115*, D13201. https://doi.org/10.1029/2009JD013276

Hudson, J. G., Noble, S., Jha, V., & Mishra, S. (2009). Correlations of small cumuli droplet and drizzle drop concentrations with cloud condensation nuclei concentrations. *Journal of Geophysical Research*, *114*, D05201. https://doi.org/10.1029/2008JD010581

Hudson, J. G., Noble, S., & Tabor, S. (2015). Cloud supersaturations from CCN spectra Hoppel minima. *Journal of Geophysical Research: Atmospheres*, *120*, 3436–3452. https://doi.org/10.1002/2014JD022669

Hudson, J. G., & Yum, S. S. (2001). Maritime–continental drizzle contrasts in small cumuli. *Journal of the Atmospheric Sciences*, *58*(8), 915–926. https://doi.org/10.1175/1520-0469(2001)058<0915:MCDCIS>2.0.CO;2

Jiang, H., Feingold, G., & Cotton, W. R. (2002). Simulations of aerosol-cloud-dynamical feedbacks resulting from entrainment of aerosol into the marine boundary layer during the Atlantic stratocumulus transition experiment. *Journal of Geophysical Research*, *107*(D24), 4813. https://doi.org/10.1029/2001JD001502

Jones, A., Haywood, J., & Boucher, O. (2009). Climate impacts of geoengineering marine stratocumulus clouds. *Journal of Geophysical Research*, *114*, D10106. https://doi.org/10.1029/2008JD011450

Joseph, J. H., Wiscombe, W. J., & Weinman, J. A. (1976). The Delta-Eddington approximation for radiative flux transfer. *Journal of the Atmospheric Sciences*, *33*(12), 2452–2459. https://doi.org/10.1175/1520-0469(1976)033<2452:TDEAFR>2.0.CO;2

Moran, K. P., Pezoa, S., Fairall, C. W., Williams, C., Ayers, T., Brewer, W. A., et al. (2012). A motion stabilized W-band radar for shipboard cloud observations and airborne studies of sea spray. *Journal of Boundary Layer Meteorology*, *143*(1), 3–24. https://doi.org/10.1007/s10546-011-9674-5

Painemal, D., Minnis, P., & O'Neill, L. (2013). The diurnal cycle of cloud top height and cloud cover over the Southeast Pacific as observed by GOES-10. *Journal of the Atmospheric Sciences*, *70*(8), 2393–2408. https://doi.org/10.1175/jas-d-12-0325.1

Painemal, D., & Zuidema, P. (2010). Microphysical variability in Southeast Pacific stratocumulus clouds: Synoptic conditions and radiative response. *Atmospheric Chemistry and Physics*, *10*(13), 6255–6269. https://doi.org/10.5194/acp-10-6255-2010

Rasch, P. J., Latham, J., & Chen, C.-C. (Jack). (2009). Geoengineering by cloud seeding: Influence on sea ice and climate system. *Environmental Research Letters*, *4*, 045112. https://doi.org/10.1088/1748-9326/4/4/045112

Seinfeld, J. H., Bretherton, C., Carslaw, K. S., Coe, H., DeMott, P. J., Dunlea, E. J., et al. (2016). Improving our fundamental understanding of the role of aerosol–cloud interactions in the climate system. *Proceedings of the National Academy of Sciences of the United States of America*, *113*(21), 5781–5790. https://doi.org/10.1073/pnas.1514043113

Snider, J. R., Leon, D., & Wang, Z. (2017). Droplet concentration and spectral broadening in Southeast Pacific stratocumulus clouds. *Journal of the Atmospheric Sciences*, *74*(3), 719–749. https://doi.org/10.1175/JAS-D-16-0043.1

Stevens, B., & Feingold, G. (2009). Untangling aerosol effects on clouds and precipitation in a buffered system. *Nature*, *461*(7264), 607–613. https://doi.org/10.1038/nature08281

Twohy, C. H., Petters, M. D., Snider, J. R., Stevens, B., Tahnk, W., Wetzel, M., et al. (2005). Evaluation of the aerosol indirect effect in marine stratocumulus clouds: Droplet number, size, liquid water path, and radiative impact. *Journal of Geophysical Research*, *110*, D08203. https://doi.org/10.1029/2004JD005116

Twomey, S. (1974). Pollution and the planetary albedo. *Atmospheric Environment*, *8*(12), 1251–1256. https://doi.org/10.1016/0004-6981(74)90004-3

Verlinden, K. L., & de Szoeke, S. P. (2018). Simulating radiative fluxes through southeastern Pacific stratocumulus clouds during VOCALS-REx. *Journal of Atmospheric and Oceanic Technology*, *35*(4), 821–836. https://doi.org/10.1175/JTECH-D-17-0169.1

Wood, R. (2006). Rate of loss of cloud droplets by coalescence in warm clouds. *Journal of Geophysical Research*, *111*, D21205. https://doi.org/10.1029/2006JD007553

Wood, R., Bretherton, C. S., Mechoso, C. R., Weller, R. A., Huebert, B., Straneo, F., et al. (2011). The VAMOS Ocean-Cloud-Atmosphere-Land Study Regional Experiment (VOCALS-REx): Goals, platforms, and field operations. *Atmospheric Chemistry and Physics Discussions*, *10*(9), 20,769–20,822. https://doi.org/10.5194/acpd-10-20769-2010

Wood, R., Leon, D., Lebsock, M., Snider, J., & Clarke, A. D. (2012). Precipitation driving of droplet concentration variability in marine low clouds. *Journal of Geophysical Research*, *117*, D19210. https://doi.org/10.1029/2012JD018305

Wyant, M. C., Bretherton, C. S., Rand, H. A., & Stevens, D. E. (1997). Numerical simulations and a conceptual model of the stratocumulus to trade cumulus transition. *Journal of the Atmospheric Sciences*, *54*(1), 168–192. https://doi.org/10.1175/1520-0469(1997)054<0168:NSAACM>2.0.CO;2

Yang, M., Huebert, B. J., Blomquist, B. W., Howell, S. G., Shank, L. M., McNaughton, C. S., et al. (2011). Atmospheric sulfur cycling in the southeastern Pacific—Longitudinal distribution, vertical profile, and diel variability observed during VOCALS-REx. *Atmospheric Chemistry and Physics*, *11*(10), 5079–5097. https://doi.org/10.5194/acp-11-5079-2011

Yum, S. S., & Hudson, J. G. (2002). Maritime/continental microphysical contrasts in stratus. *Tellus Series B: Chemical and Physical Meteorology*, *54*(1), 61–73. https://doi.org/10.1034/j.1600-0889.2002.00268.x

Zheng, X., Albrecht, B., Minnis, P., Ayers, K., & Jonson, H. H. (2010). Observed aerosol and liquid water path relationships in marine stratocumulus. *Geophysical Research Letters*, *37*, L17803. https://doi.org/10.1029/2010GL044095

Zuidema, P., Leon, D., Pazmany, A., & Cadeddu, M. (2012). Aircraft millimeter-wave passive sensing of cloud liquid water and water vapor during VOCALS-REx. *Atmospheric Chemistry and Physics*, *12*(1), 355–369. https://doi.org/10.5194/acp-12-355-2012

Zuidema, P., Westwater, E. R., Fairall, C., & Hazen, D. (2005). Ship-based liquid water path estimates in marine stratocumulus. *Journal of Geophysical Research*, *110*, D20206. https://doi.org/10.1029/2005JD005833

## Erratum

In the originally published version of this paper, a number of lowercase letter l's were replaced with lowercase letter i's. The errors have since been corrected, and this version can be considered the authoritative version.